PHYSICAL REVIEW B **109**, 174523 (2024)

Magnetic and structural properties of the iron silicide superconductor LaFeSiH

M. F. Hansen,[1,2] S. Layek,[1,3] J.-B. Vaney,[4] L. Chaix,[1] M. R. Suchomel,[4] M. Mikolasek,[5] G. Garbarino,[5] A. Chumakov,[5] R. Rüffer,[5] V. Nassif,[1,6] T. Hansen,[6] E. Elkaim,[7] T. Pelletier,[8] H. Mayaffre,[8] F. Bernardini,[9] A. Sulpice,[1] M. Núñez-Regueiro,[1] P. Rodière,[1] A. Cano,[1] S. Tencé,[4] P. Toulemonde,[1] M.-H. Julien,[8] and M. d'Astuto[1]

[1]*CNRS, Université Grenoble Alpes, Institut Néel, 38042 Grenoble, France*
[2]*Earth and Planets Laboratory, Carnegie Institution for Science, 5241 Broad Branch Road, NW, Washington, DC 20015, USA*
[3]*Department of Physics, School of Advanced Engineering, University of Petroleum and Energy Studies, Dehradun, Uttarakhand 248007, India*
[4]*Université Bordeaux, CNRS, Bordeaux INP, ICMCB, UMR 5026, F-33600 Pessac, France*
[5]*ESRF-The European Synchrotron, CS40220, 38043 Grenoble Cedex 9, France*
[6]*Institut Laue-Langevin, 71 Avenue des Martyrs, 38000 Grenoble, Cedex 9, France*
[7]*Synchrotron SOLEIL, L'Orme des Merisiers, 91190 Saint Aubin, France*
[8]*CNRS, LNCMI, Université Grenoble Alpes, INSA-T, UPS, EMFL, 38042 Grenoble, France*
[9]*Dipartimento di Fisica, Università di Cagliari, Cittadella Universitaria, I-09042 Monserrato (CA), Italy*

(Received 23 August 2023; revised 23 March 2024; accepted 25 March 2024; published 21 May 2024)

The magnetic and structural properties of the recently discovered pnictogen/chalcogen-free superconductor LaFeSiH have been investigated by ^{57}Fe synchrotron Mössbauer source spectroscopy, X-ray and neutron powder diffraction, and ^{29}Si nuclear magnetic resonance spectroscopy. In contrast with earlier work suggesting the presence of an orthorhombic and magnetic ground state as in underdoped Fe-based pnictides, our results unambiguously establish that LaFeSiH is in fact similar to strongly overdoped Fe-based pnictides: there is no magnetic order (including under hydrostatic pressure up to 18.8 GPa), nor even fluctuating local moments and the system remains tetragonal down to 2 K. This raises the prospect of enhancing the T_c of LaFeSiH by reducing its carrier concentration through appropriate chemical substitutions.

DOI: 10.1103/PhysRevB.109.174523

I. INTRODUCTION

Fe-based superconductors form a rich and complex family of unconventional superconducting materials [1–3]. In their parent phases, these systems generally display a distinctive structural transition from tetragonal to orthorhombic symmetry triggered by electronic degrees of freedom (the so-called nematic order). In many compounds such as the arsenide LaFeAsO, this structural transition is manifestly tied to the subsequent emergence of stripe-type antiferromagnetic (AFM) order [4–6]. Furthermore, these orders appear to be in competition with superconductivity in the sense that, in order to promote the latter, they need to be suppressed by doping, for example. Still, there are cases such as $Ba(Fe_{1-x}Co_x)_2As_2$ and $(Ba_{1-x}K_x)Fe_2As_2$ in which coexistence has been observed. The global phase diagram of the Fe-based superconductors thus reveals a generic interplay between magnetism and superconductivity in these systems.

Here, we address whether this interplay emerges also in the comparatively recent crystallogenide LaFeSiH [7]. This system is the representative material of a new subfamily of FeSi-based superconductors [8,9]. LaFeSiH itself is one of the very few Fe-based materials that displays superconductivity in its parent phase [7], which cannot be explained by the conventional electron-phonon pairing mechanism [10]. Also, magnetic penetration depth measurements suggest that the superconducting gap has d-wave symmetry [11].

Interestingly, the crystal structure of this system has been reported to be tetragonal at room temperature and orthorhombic at 15 K and $\approx$0.1 GPa, with a peculiar reentrant behavior under further pressurization [7]. This would be consistent with the AFM order obtained from first-principles calculations [7,12], suggesting that LaFeSiH could be a unique example of a Fe-based parent compound in which superconductivity coexists with additional orders in contrast with other systems in which this is realized upon doping only. At the same time, it is known that similar calculations tend to overestimate the tendency towards magnetic order in previous Fe-based superconductors and that such order may be suppressed by fluctuations in metals near quantum critical points (see, e.g., Ref. [13]). Thus, it is important to verify the actual experimental situation in the case of this new crystallogenide.

In this paper we investigate the magnetic properties of LaFeSiH as a function of temperature, magnetic field, and pressure using ^{57}Fe synchrotron Mössbauer source (SMS) spectroscopy, neutron powder diffraction (NPD), and nuclear magnetic resonance spectroscopy (NMR). In addition, we revisit the crystal structure of this compound by means of both neutron and X-ray diffraction (XRD). Within the detection limits of these techniques, we find no evidence of neither lattice distortion down to 2 K, long-range magnetic order, nor Fe local moments. The upper bound on the ordered moment is on the order of $10^{-2}\,\mu B$, which is well below the calculated value $m(\mathrm{Fe}) = 1.16\,\mu_B$ [7]. Furthermore, we find no evidence of pressure-induced magnetism up to 18.8 GPa from SMS spectroscopy. The absence of magnetism together with the temperature dependence of the NMR relaxation rate $1/T_1$ suggest that the parent LaFeSiH should be regarded as a (self-)overdoped compound.

II. METHODS

A. Samples

LaFeSi precursor powders were first prepared by arc melting of a stoichiometric mixture of pure elements (La, Fe, and Si), subsequently ground, compacted, and subjected to a thermal treatment of 7 days at 950 °C. The final LaFeSiH powders were obtained from the hydrogenation of the precursors, treated at 250 °C for 4 h under a static pressure of gaseous H_2 of 10 bars. The deuterated sample, LaFeSiD, for the NPD experiment was obtained with a similar protocol, hydrogen gas being replaced by deuterium gas in the last stage (see also Ref. [14]). For the preparation of LaFeSiH single crystals, small single crystals of LaFeSi were separated from the bulk of an arc-melted Si-under-stoichiometric $\mathrm{LaFeSi}_{0.86}$ composition. The 20-µm-thick plate-like single crystals of various sizes were then hydrogenated at 250 °C under a flow of H_2 gas for 4 h. Both the LaFeSiH powders and single crystals were checked by X-ray diffraction and refinement of the unit-cell parameters were found to be in good agreement with previously reported data [7]. For the SMS measurements, additional samples were synthesized using 96% isotopic ^{57}Fe instead of the naturally abundant isotope. Bulk superconductivity was confirmed by measuring the magnetization of all samples showing $T_c = 8.5$–10 K, consistent with previous reports [7], as described in Appendix C. Furthermore, the superconducting state was verified using resistivity measurements for the isotope enriched sample, showing $T_c \approx 10\,\mathrm{K}$, again, consistent with previous reports [7], as described in Appendix B.

B. Synchrotron Mössbauer source spectroscopy under pressure and magnetic field

To probe the magnetic phase diagram of LaFeSiH at both ambient and high pressure, we used SMS spectroscopy. Compared with standard laboratory-source Mössbauer spectroscopy [15] or nuclear forward scattering [16], SMS spectroscopy is relatively a new technique that has the advantage of having a very focused beam [17–19]. Thus, in addition to low temperature and high magnetic field, this feature enables high-pressure experiments [20]. Specifically, we used the ^{57}Fe SMS spectroscopy [20,21] at the Nuclear Resonance beamline (ID18) [22] of the European Synchrotron Radiation Facility (ESRF, Grenoble), where this technique was developed. Data analysis was carried out with the MossA procedure of Matlab© [23].

The $^{57}\mathrm{FeBO}_3$ crystal was set in the (111) reflection and sinusoidal acceleration configuration as described in Ref. [20]. Energy calibrations were performed for each velocity configuration of the Doppler spectrometer, using a 25-µm-thick natural α-iron absorber standard. We used a maximum velocity of 11.30(2) mm/s for the first set of measurements, at low field and ambient pressure, and 5.64(1) mm/s for the remaining measurements. We measured two samples, one with isotope-enriched iron and one with natural iron. This is further detailed in Appendix A.

For all measurements the cryomagnet system of the beamline was used, providing temperatures between 2 and 300 K and an external magnetic field between −8 and +8 T in the vertical direction. The system is equipped with aluminum windows for the γ-ray beam and quartz windows for the ruby fluorescence calibration signal. Pressure calibration was performed *in situ* after each change of pressure and/or temperature conditions.

A membrane-driven diamond-anvil cell (DAC) with 500 µm culet diamonds and stainless steel gasket was used. The enriched and natural sample were loaded into the same DAC used for the temperature and field measurements at ambient pressure (as can be seen in Fig. 8 in Appendix A), using He as a pressure-transmitting medium. Using an optics system with a very long working distance (f $\frac{1}{28}$ 50 cm) we measured *in situ* the ruby fluorescence for pressure calibration.

C. Diffraction techniques

Neutron powder diffraction (NPD) was carried out at the D2B powder diffraction instrument of the Institute Laue Langevin (ILL) using a wavelength of $\lambda = 1.5944$ Å. The deuterated sample, LaFeSiD, was inserted in a cylindrical vanadium sample holder and measured at 10 fixed temperature points in the 10–300 K range with an exposure time of ≈2 h per point and ≈4 h at 2 K. The empty cryostat was also measured, showing only one significant background peak at 151.2°. X-ray powder diffraction (XRD) was carried out at the CRISTAL beamline of the synchrotron SOLEIL in the temperature range 5–300 K. The sample was loaded in a 300-µm-diameter borosilicate capillary. Two different detectors were used in parallel for each: a fast photon counting strip detector (Mythen2) for medium angular resolution but excellent counting statistics acquisition and a multicrystal analyzer for high angular resolution and medium counting statistics acquisition. Precise lattice parameters were determined using the multicrystal analyzer data and the accurate atomic positions were obtained from refinements of the Mythen2 data. The wavelength used for the experiment was $\lambda = 0.51302$ Å. The collected data were corrected for absorption using a µR value of 1.23. XRD and NDP results are compared in Appendix D.

D. Nuclear magnetic resonance

^{29}Si NMR experiments were performed as a function of temperature down to 2.85 K in an external field of ≈15 T (the exact field value is calibrated from the ^{63}Cu NMR resonance frequency in metallic Cu). At this field, the superconducting transition is not detected in our measurements so only the normal state is probed here. We measured three NMR observables:

(1) We measured the magnetic hyperfine shift K, also called the Knight shift, which is calculated from the frequency

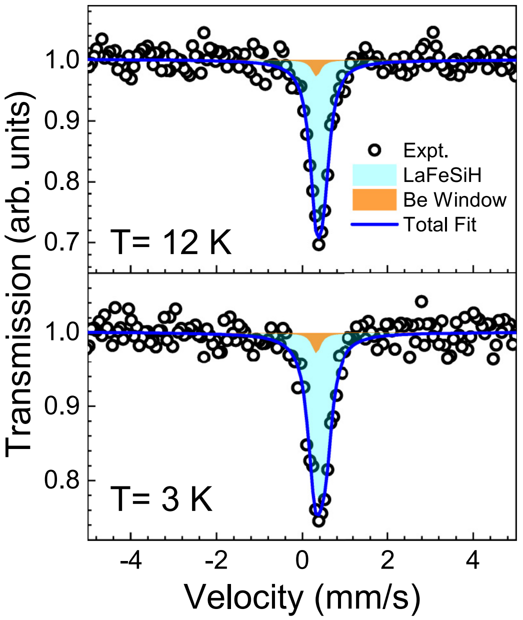

FIG. 1. Synchrotron ^{57}Fe Mössbauer of LaFeSiH natural iron sample at 3 K (superconducting state) and 12 K (normal state) at ambient pressure. Empty circles represent experimental data points. The Mössbauer spectra are fitted with single line (cyan fill) plus an additional contribution, also modeled with a single line (orange fill) coming from iron impurities in the Beryllium window and collimating lenses of the beamline. The blue solid line through the data points represents the overall fit convoluted with the instrumental resolution.

difference between the measured ^{29}Si resonance and the calculated resonance of the bare nucleus. K is usually written as the sum of a T independent orbital part and a temperature dependent spin part: $K = K_{\rm orb} + K_{\rm spin}$, where $K_{\rm spin}$ is proportional to the local uniform ($q = 0$) and static ($\omega = 0$) spin susceptibility $\chi_{\rm spin}$.

(2) We measured the linewidth, providing a measure of the spatial distribution of hyperfine shifts that may result from chemical, lattice and electronic inhomogeneity on all length scales. In a random powder, the Knight shift anisotropy also contributes to the linewidth but since the lineshape does not show any shoulder or splitting here [Fig. 6(a)], the line broadening turns out to be rather dominated by spatial inhomogeneity. The lineshape has been fit by a Voigt profile; that is, a convolution of Gaussian and Lorentzian functions of widths w_G and w_L, respectively, giving a full width at half maximum FWHM $= 0.5346\, w_L + (0.2166\, w_L^2 + w_G^2)^{1/2}$.

(3) We measured the spin-lattice relaxation rate, T_1^{-1}, providing information on low-energy spin dynamics through the imaginary part of the dynamic spin susceptibility: $(T_1T)^{-1} \propto \sum_q A_\perp^2(q)\chi_\perp''(q,\omega_n)$, where ω_n is the nuclear Larmor frequency ($\approx 10^8$ Hz here) and $A(q)$ is a site-specific hyperfine form factor. T_1 values were determined from single-exponential fits of the time dependence of the nuclear magnetization following a saturating pulse. Excellent fits were obtained at all temperatures, without introducing any stretching exponent.

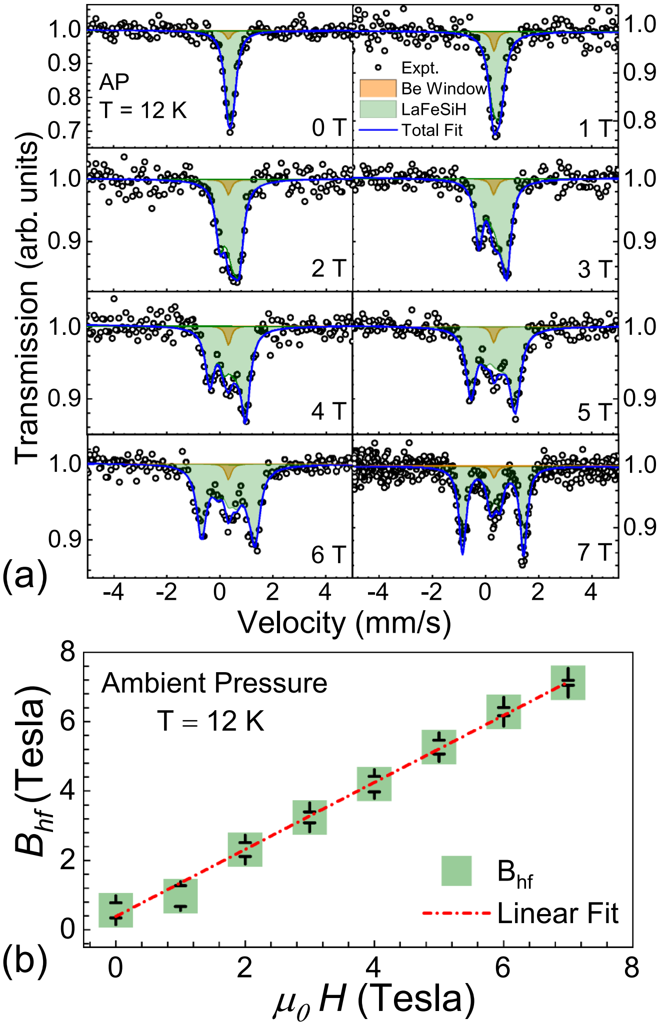

FIG. 2. (a) Empty black circles represent SMS spectra of LaFeSiH natural iron sample at ambient pressure and 12 K at different applied magnetic field from μ_0H = 0 to 7 T whereas the blue solid line through the data points represents the overall fit convoluted with the instrumental resolution. Mössbauer spectra were fitted with a magnetic splitting (green) plus a single line, orange filled, coming from iron impurities in Beryllium window and collimating lenses of the beamline. (b) The extracted hyperfine field $B_{hf}(T)$ (green squares), compared with a linear fit (red dot-dashed line).

III. EXPERIMENTAL RESULTS AND DISCUSSION

A. Synchrotron Mössbauer source spectroscopy

In Fig. 1, we show SMS spectra of ^{57}Fe isotope in LaFeSiH taken at low temperature, at 12 and 3 K, at ambient pressure and without any applied magnetic field (raw data are shown in Fig. 7, see Appendix A). The spectra was well fit by a single line, with possible quadrupolar splitting, at best of the same order of the resolution, of about 0.1 mm/s, also indicating a very weak electric field gradient on the iron site. A single lineshape does not necessarily mean that the corresponding magnetic moment is zero. Taking into account the instrumental linewidth as well as the broadening due to distributions such as isomer shift and quadrupole splitting, the data may be compatible with a very small value. Within the experimental

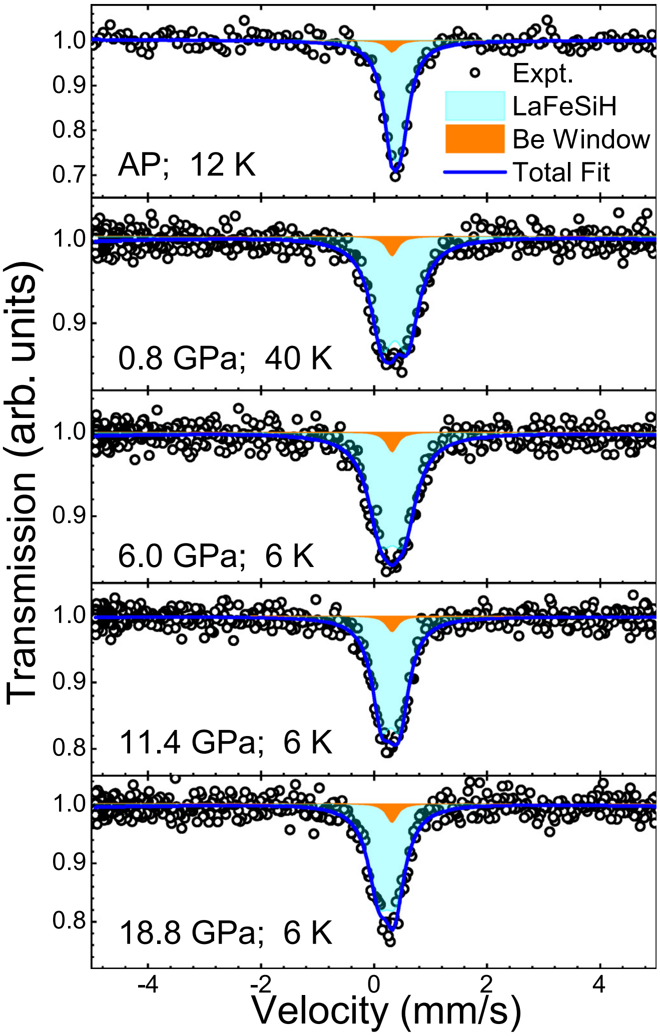

FIG. 3. Synchrotron ^{57}Fe Mössbauer spectra of LaFeSiH natural iron sample as a function of pressure up to 18.8 GPa, in zero field and at the lowest temperature for each pressure point. Exact values of pressure and temperature are written in the respective plots. For each pressure, the temperature of the data shown is always above the superconducting one. Note that the data at ambient pressure are taken outside the DAC cell. The same symbols and color code are used as in Fig. 1.

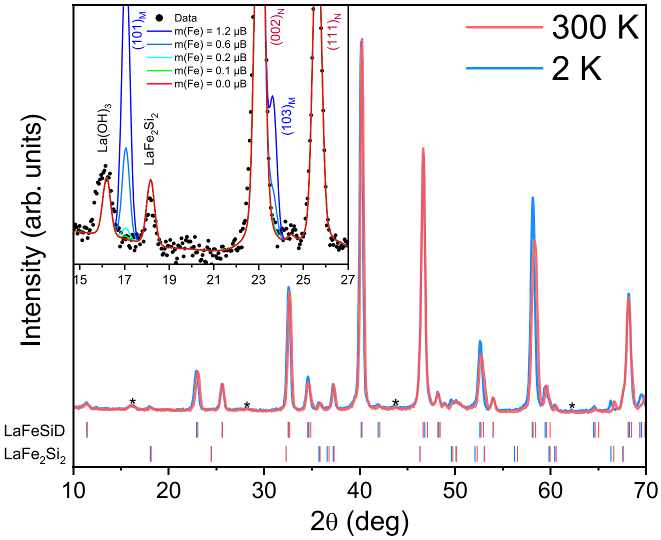

FIG. 4. Neutron powder diffraction patterns at 300 K (in red) and 2 K (in blue) recorded at the D2B instrument at the ILL. No additional peaks are observed between the two temperatures, consistent with the lack of long-range magnetic ordering with $k \neq 0$. Peaks indicated by a star originate form a small La(OH)$_3$ impurity. Inset shows neutron powder diffraction pattern measured at 2 K. Simulations of the single stripe AFM structure contribution is plotted on top of the data, with different magnetic moment values ranging from $m(\mathrm{Fe}) = 1.2\,\mu_B$ (blue) to $m(\mathrm{Fe}) = 0.1\,\mu_B$ (green).

resolution, then the measured magnetic hyperfine field can be estimated to be just lower than ≈ 0.6 T.

Without any assumption about the magnetic state of the system, it is difficult to estimate the Fe magnetic moment that would correspond to that hyperfine field. We note that the measured signal is similar to what is reported for LaFeAsO$_{0.89}$ F$_{0.11}$ [24] and in FeSe [25], which both display no magnetic order. In the case of LaFeAsO with single-stripe AFM order, the hyperfine magnetic field B$_{hf}$ has been reported to be 4.86 T at 13 K [26] and 5.25 T at 4.2 K [24,27]. These values correspond to a Fe magnetic moment $m_{\mathrm{Fe}} = 0.25(5)\,\mu_B$–$0.35\,\mu_B$. According to our data, the upper bound of the hyperfine field in LaFeSiH is much lower so that, assuming the same type of AFM order as in LaFeAsO, the Fe magnetic moment then should be $\lesssim 0.04\,\mu_B$. This difference is striking since the calculated moment is $\gtrsim 1.2\,\mu_B$ in both LaFeAsO and LaFeSiH [7,13].

To further investigate the local Fe moment, we applied a magnetic field, μ_0H, up to 7 T. In Fig. 2(a) we show the results ramping up from zero to 7 T for the natural iron sample at 12 K and ambient pressure. Similar results where obtained for the field downstroke on the enriched iron sample. At the maximum field, 7 T, an additional measurement on a second enriched sample gave the same B$_{hf}$ within error bars. In Fig. 2(b) we show the fitted B$_{hf}$ as a function of the applied field μ_0H, fitted by linear regression. The small deviation from the applied field is constant on all the data points for the field upstroke, resulting in an intercept of 0.038 ± 0.03 T. Our fit gives a slope of 0.97 ± 0.06, consistent with unity within the error bars (3σ), pointing to an effect coming exclusively from the applied field without any contribution from a molecular field acting on the ^{57}Fe nuclei. A similar observation was made for LaFeAsO$_{0.89}$ F$_{0.11}$ [24], which also shows a hyperfine field at 4.2 K corresponding within error bars to the applied external field at 7 T.

We note that measurements performed during applied field downstroke on enriched iron sample with 96% ^{57}Fe, give results that are perfectly superposed to the upstroke between 5 and 7 T, i.e., as long as a magnetic splitting is larger than the intrinsic linewidth, which is larger for the enriched iron sample because of its broadened signal compared with a natural iron sample.

We then applied a similar procedure on the same sample, loaded in the high-pressure diamond-anvil cells as described in Sec. II B. We investigated the Mössbauer signal up to 18.8 GPa and down to 6 K, where we only performed

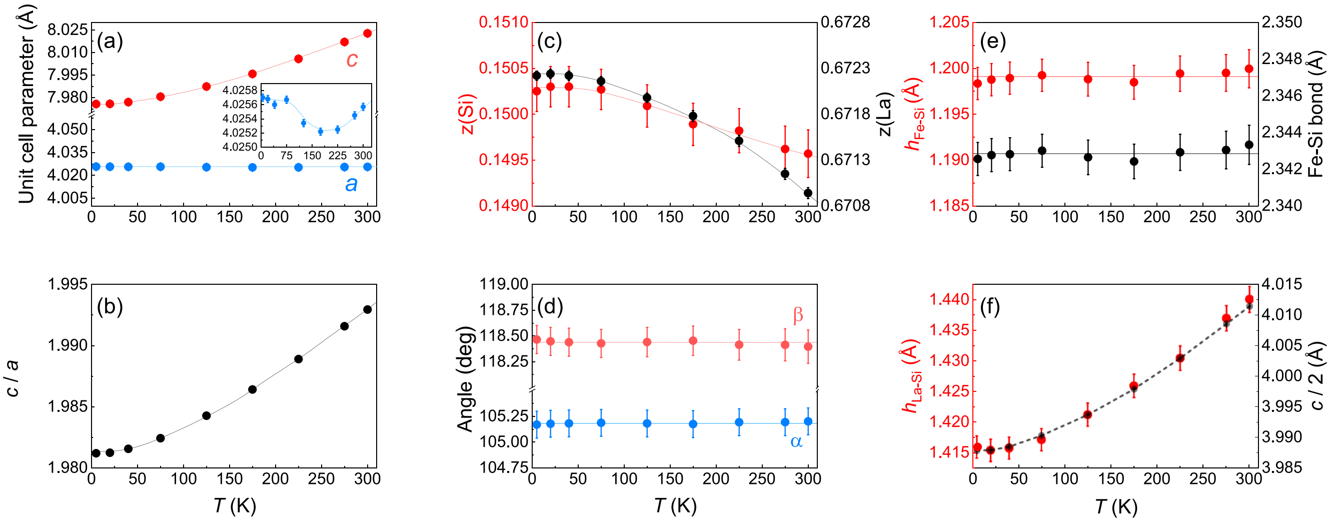

FIG. 5. The refined structural parameters as a function of temperature, obtained from synchrotron X-ray diffraction (at the CRISTAL beamline at SOLEIL). (a) The unit-cell parameters a and c. (b) The unit-cell parameter ratio c/a. (c) The fractional z coordinates of Si and La. (d) The $FeSi_4$ tetrahedra angles α and β. (e) The Fe-Si height and bond length. (f) In red, the La-Si height. In black, $c/2$. This displays the contraction mechanism upon cooling.

zero-field measurements, before breaking the diamonds while attempting to reach higher pressure. A summary of the results is shown in Fig. 3. In LaFeAsO, pressure monotonically decreases both T_N and B_{hf}, while initially increasing T_c from zero up to ≈20 K at about 10 GPa [28]. The results shown here in LaFeSiH are similar to those at ambient pressure, although a broadening is now observed, that can be fitted with a residual hyperfine field at zero applied field. However, we found that all measurements in the cell give a large broadening of the lineshape, possibly due to vibration of the high-pressure membrane DAC as well as a distribution of the pressure inside the sample. In particular, for the highest pressure at zero field, we estimate a maximum possible hyperfine field of 1.3 ± 0.3 T, larger than the value found in samples outside the DAC cell, but with a lineshape that can be perfectly interpreted as coming from a single line.

In summary, the Mössbauer data shows no clear splitting of the nuclear resonance that could be associated with the hyperfine magnetic field which would result from the magnetic polarization of the electronic cloud on the iron sites. This rules out standard magnetic states (either ordered or disordered) in which the Fe magnetic moment is $\gtrsim 0.25\,\mu_B$, although lower values cannot be excluded. Also, the present results cannot rule out complex orders whose symmetry could reduce the hyperfine field. In this respect, we note that a very small moment, below $m_{\text{Fe}} \approx 0.05\,\mu_B$, in a disordered state, could possibly be probed using X-ray emission spectroscopy, looking at the K_β line satellite, a very sensitive probe to partially filled $3d$ electronic band, as recently shown in ϵ iron [29] and FeSe [30]. Another possibility would be to use synchrotron radiation perturbed angular-correlation spectroscopy, another approach recently applied to ϵ iron [31].

B. Neutron powder diffraction

Figure 4 shows the NPD patterns obtained from LaFeSiH at 300 K and 2 K (see also Appendix D). As we see, the difference between these two patterns is simply the shift of the peaks with neither additional Bragg peaks nor peak splitting appearing at low temperatures. Thus, the observed change can be fully ascribed to the thermal contraction of the lattice with no indication of either structural symmetry breaking or development of long-range magnetic order (apart from relative changes due to the thermal contraction and/or small changes of the relative atomic positions, no extra intensity is observed on top of the nuclear diffraction peaks).

To estimate the detection limit of the Fe magnetic moment m_{Fe} of potential long-range magnetic order in this NPD experiment, we performed several simulations assuming the single-stripe-type AFM order, as suggested from first principles calculations [7,12], and usually encountered in the "1111-type" arsenides [32]. In these simulations, different values of m_{Fe} from $1.2\,\mu_B$ to $0.1\,\mu_B$ were considered. The accompanying orthorhombic distortion was also considered, assuming the value $\delta = (b-a)/(b+a) \approx 2\times10^{-3}$ suggested in Ref. [7] (i.e., from measurements carried out in a diamond-anvil cell at 15 K and ≈0.1 GPa). The red curve in the inset of Fig. 4 shows the nuclear signal of the calculated diffraction pattern from the Rietveld fit of the observed pattern collected at 2 K. By comparing our simulations to the noise level of the data, we conclude that single-stripe AFM order with $m_{\text{Fe}} \leqslant 0.15(5)\,\mu_B$ would not be detected in our experiment.

C. X-ray powder diffraction

To confirm the absence of structural distortion, we performed XRD experiments with higher angular resolution, as a function of temperature (see Fig. 16 in Appendix D). No splitting or additional peaks related to lowering of symmetry were found at low temperature.

Thus, we find no evidence of tetragonal to orthorhombic distortion of the LaFeSiH crystal structure. The absence of

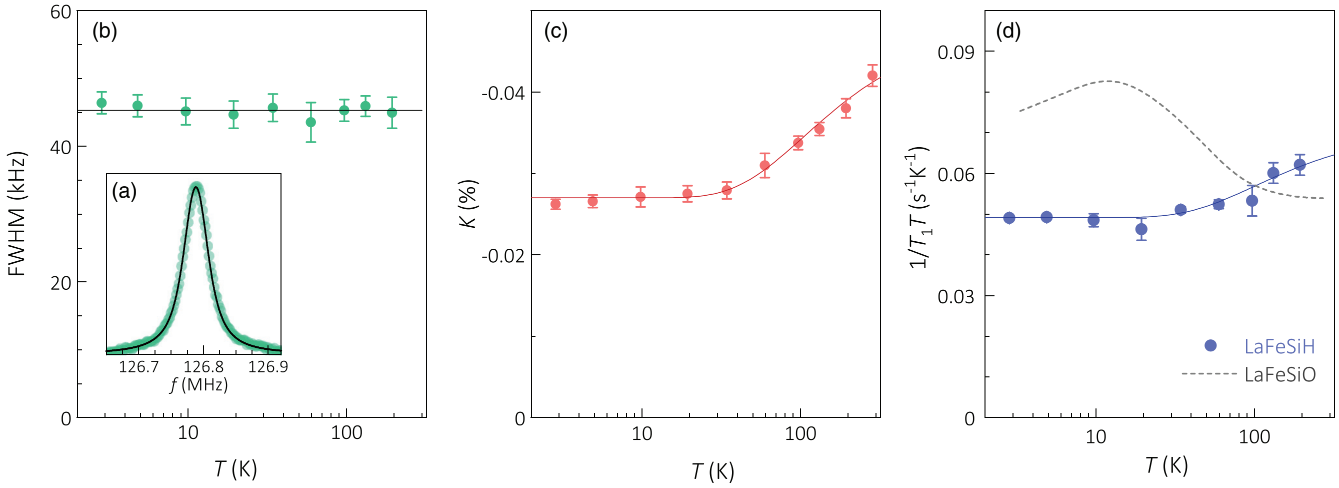

FIG. 6. (a) ^{29}Si NMR line (green) in a field of ≈15 T and $T = 2.85$ K. The line is a fit to a Voigt profile. (b) Full width at half maximum (FWHM). The horizontal line is a fit to a constant value 45 ± 3 kHz. (c) Total magnetic hyperfine shift K. The solid trace is a fit to an activated dependence with a gap value $\Delta_K = 106 \pm 24$ K. The negative sign of K with larger absolute values at high temperatures shows that the hyperfine coupling of ^{29}Si is negative. (d) Spin-lattice relaxation rate T_1^{-1} divided by T. The solid trace is a fit to an activated dependence with a gap value $\Delta_{T_1} = 101 \pm 38$ K $\approx \Delta_K$. For comparison purpose, the dashed trace shows $(T_1T)^{-1}$ data in LaFeSiO [9]. While the values are similar, the T dependence is very different, which is attributed to magnetic fluctuations in LaFeSiO.

such a distortion is confirmed in a complementary Raman spectroscopy study [33]. In Ref. [7], an orthorhombic distortion was concluded from (i) the equation of state (normalized stress as a function of Eulerian strain) and (ii) the asymmetric broadening of e.g., the (220) peak measured under pressure, which were observed to display the same re-entrant behavior as the magnetically induced distortion obtained from first-principles calculations (see Appendix E for additional details). That behavior, however, may be the result of chemical inhomogeneity of the LaFeSiH phase (i.e., with a small range of nonstoichiometry) or the presence of secondary phases in the previous samples, which at the time were not optimized to the sample quality presented in the present study.

Thus, we assume the tetragonal $P4/nmm$ model to further analyze the temperature dependence of the crystal structure. Figure 5(a) shows the refined lattice parameters a and c obtained from Rietveld fits of the corresponding XRD data. As we see, the thermal contraction of the lattice is clear from the behavior of the c parameter. The a parameter, however, remains essentially constant except for a minute broad dip at 175 K [see inset in 5(a)]. This dip, which is also observed in the NPD data (see Appendix D), cannot be readily explained although it may be related to the coupling between structural and electronic degrees of freedom. The anisotropy of the thermal contraction is further illustrated in Fig. 5(b). Figure 5(c) shows the parameters z(Si) and z(La) that determine the Si and La positions within the unit cell as a function of temperature. The resulting Fe-Si height and Fe-Si bond length are shown in Fig. 5(e). As we see, these latter quantities remain essentially constant. Furthermore, Figs. 5(d) and 5(f) show the angles associated with the FeSi$_4$ tetrahedra and the La-Si height, respectively. The latter essentially tracks the decrease in c [see right axis in Fig. 5(f)]. When it comes to local environment of the Fe atoms, it remains virtually unchanged as a function of temperature.

D. Nuclear magnetic resonance

In general, magnetic order has two main effects on NMR observables: (1) It shifts, splits or broadens the NMR lines (except in those exceptional cases where the hyperfine field vanishes at the nucleus position for symmetry reasons, which should not be the case for ^{29}Si here). (2) It produces a sharp change in the spin-lattice relaxation rate T_1^{-1}, either an abrupt drop upon entering the ordered state if the transition is first order or a peak at the transition temperature if the transition is second order (and also a peak for a continuous freezing).

None of these features are observed in our ^{29}Si NMR data in LaFeSiH: all observables show weak and smooth temperature dependence (Fig. 6), which thus rules out the presence of magnetic order.

Both the Knight shift K [Fig. 6(c)] and $(T_1T)^{-1}$ [Fig. 6(d)] decrease smoothly upon cooling and saturate to a constant value below ≈20 K. Notably, there is no enhancement of $(T_1T)^{-1}$ upon cooling. In fact, the T dependence of both K and $(T_1T)^{-1}$ is consistent with a thermal-activation form and a fit to $a + b\exp(-\Delta/k_BT)$ yields virtually identical gap values in K ($\Delta_K = 106 \pm 24$ K) and in T_1 ($\Delta_{T_1} = 101 \pm 38$ K), respectively. Notice that a fit with Δ_{T_1} fixed to $2\Delta_K$, as observed in LaNiAsO$_{1-x}$F$_x$ [34], degrades the fit goodness (reduced chi-squared of 1.3 instead of 0.6).

At the qualitative level, the exponential dependence of both K and $(T_1T)^{-1}$ over the whole T range is typical of strongly overdoped Fe-based superconductors [34–36]. At the quantitative level, our data strikingly resemble results in strongly overdoped Ba(Fe$_{1-x}$Co$_x$)$_2$As$_2$ for which the activated $(T_1T)^{-1}(T)$ with $\Delta_{T_1} \simeq \Delta_K$ has been ascribed to spin fluctuations involving small momentum transfers (so-called "intraband" scattering) [37]. This contribution is also present in the underdoped regime but it becomes increasingly masked upon cooling as the growth of $(\pi, 0)$ spin fluctuations ("interband" scattering) leads to a large upturn in $(T_1T)^{-1}$ [38,39]. Such stripe-type spin fluctuations are manifestly absent in LaFeSiH. The similarity with overdoped Fe pnictides gains further support from the observation that the change in T_1 (in both magnitude and T dependence) from LaFeSiH to LaFeSiO [Fig. 6(d)] is very similar to the change observed in $\mathrm{LaFeAsO}_{1-x}\mathrm{F}_x$ when F doping increases from $x = 0.08$ to $x = 0.10$ [40].

Moreover, the constant linewidth from room temperature down to 2.8 K [Fig. 6(b)] and the absence of stretched-exponential behavior of the magnetization recovery in T_1 measurements are both typical of spatially homogeneous systems with negligible electronic correlations (the conjunction of electron correlations and unavoidable disorder tends to broaden the NMR lines upon cooling). In the sister compound LaFeSiO, even moderate antiferromagnetic correlations induce line broadening and stretched-exponential behavior [9]. The constant linewidth here is also consistent with the absence of an orthorhombic transition inferred from XRD (orthorombicity differentiates K values along a and b axes, which splits the NMR lines, see Ref. [41] and references therein). However, the relatively large width in the powder sample obviously makes NMR a much less sensitive probe than XRD in the present case, and our data cannot exclude small and/or short-range distortions due to pinned nematic fluctuations [42].

It is noteworthy that K values are negative and increasingly so at high T [Fig. 6(c)], which is consistent with a negative hyperfine coupling ^{29}A for ^{29}Si. This contrasts with the positive coupling found in the sister compound LaFeSiO [9]. Deferring the calculation of hyperfine fields to a subsequent work, we still remark that absolute values of ^{29}A must be similar in LaFeSiH and LaFeSiO since $|K|$ values are similar (varying between 0.01 and 0.02% in LaFeSiO). It is then reasonable to assume that $|^{29}A| \simeq |^{31}A| = 0.61\ \mathrm{T}/\mu_B$ for ^{31}P in $\mathrm{BaFe}_2(\mathrm{As}_{1-x}\mathrm{P}_x)_2$ [43], so that we can compare NMR results in the two systems. For $x \simeq 0.3$ in the latter compound, ordered moments as small as $0.05\ \mu_B$ lead to T_1 results for ^{31}P [43,44] that are very different from those reported here for ^{29}Si. This indicates that there is no ordered moment greater than a small fraction of $\approx 0.05\ \mu_B$ in LaFeSiH. In fact, with a detection limit set by our spectral linewidth of 45 kHz, we derive an upper bound of $\approx 0.01\ \mu_B$ for a putative ordered moment.

The NMR data thus unambiguously show that LaFeSiH has neither spin order nor even local moments with stripe-type AFM fluctuations. The Fermi surface of LaFeSiH is very likely similar to that of strongly overdoped iron pnictides. This raises the prospect of enhancing the T_c of LaFeSiH by appropriate chemical substitutions. These results also contribute to establishing a solid, quantitative phenomenology of NMR data in overdoped Fe-based superconductors that could be confronted with theoretical predictions based on realistic band structures.

IV. CONCLUSIONS

We have carried out a detailed investigation of the magnetic and structural properties of the Fe-based crystallogenide superconductor LaFeSiH by means of synchrotron Mössbauer spectroscopy, nuclear magnetic resonance spectroscopy, and neutron and X-ray powder diffraction experiments as a function of temperature and pressure. The data reveals no sign of either long-range magnetic order or local magnetic moments, with an upper bound of $0.01\ \mu_B$–$0.04\ \mu_B$ for the Fe moment according to the detection limit. Besides, the crystal structure is found to remain tetragonal down to 2–5 K at ambient pressure on the basis of neutron and X-ray diffraction. In this respect, the parent LaFeSiH superconductor can be regarded as analogous to previous Fe-based superconductors in their overdoped regimes.

ACKNOWLEDGMENTS

We thank M.-A. Méasson, I. Vinograd, and R. Zhou for discussions. Part of this work was performed at the LNCMI, a member of the European Magnetic Field Laboratory (EMFL). This work was supported by the ANR-18-CE30-0018-03 Ironman grant and the French State funds ANR-10-LABX-51-01 (Labex LANEF du programme d'Investissements d'Avenir) We acknowledge the European Synchrotron Radiation Facility (ESRF) for provision of synchrotron radiation resources at the ID18 Nuclear Resonance beamline. We acknowledge the synchrotron SOLEIL for providing synchrotron radiation resources at the beamline (experimental report: 20191508). We acknowledge the Institute Laue Langevin (ILL) for providing neutron radiation at the D2B [45].

APPENDIX A: SYNCHROTRON MÖSSBAUER SOURCE SPECTROSCOPY: ADDITIONAL INFORMATION

We measured seven crystals at ambient pressure, two with natural iron, and the remaining five highly enriched in ^{57}Fe. Based on these measurements we selected two of them, one with 96% ^{57}Fe substitution and the one with natural iron. The central shift and linewidth of the SMS radiation was measured using a single-line $\mathrm{K}_2\mathrm{Mg}^{57}\mathrm{Fe(CN)}_6$ absorber, typically before and after each measurement point. From those measurements the actual center shift and energy resolution of the SMS was derived for the data evaluation of the spectra. Typically, values are 0.395 ± 0.10 mm/s for the center shift with respect to α-Fe and 0.25 ± 0.05 mm/s for the energy resolution. The beam from the SMS was focused using a Kirkpatrick-Baez mirror to the spot size of 16 µm × 18 µm (vertical × horizontal, FWHM). After a first measurement made on all samples at the lowest temperature (about 3 K), ambient pressure and zero magnetic field, for comparison and reproducibility check, we selected two of them, one with 96% ^{57}Fe substitution (hereafter named "enriched iron sample") and the one with natural iron (hereafter named "natural iron sample"), for the remaining experiments in temperature and field. The choice was made on the basis of the smallest width of the line, corresponding to the best quality (e.g., lower disorder) of the crystal. Samples with 96% ^{57}Fe substitution experienced mainly line broadening due to their high effective thickness, while the natural sample gave a resolution limited broadening, although requiring longer accumulation times.

TABLE I. The refined structure of LaFeSiH at $T = 300$ K and $T = 5$ K as measured using XRD.

$P4/nmm$, setting 2						
	$T = 300$ K			$T = 5$ K		
	$a = 4.02557(1)$ Å, $c = 8.0227(5)$ Å			$a = 4.02570(2)$ Å, $c = 7.9756(6)$ Å		
Atom	x	y	z	x	y	z
La	0	0.5	0.6709(4)	0	0.5	0.6722(4)
Fe	0.5	0.5	0.5	0.5	0.5	0.5
Si	0.5	0	0.1495(7)	0.5	0	0.1502(6)
H	0	0	0	0	0	0

In Fig. 7 we show the raw data of Fig. 1, taken with an acquisition time of about 10^3 s.

In Fig. 8 we show a picture of the enriched (S #4) and natural (S #7) samples loaded in a DAC with 500 μm culet diamonds and a stainless-steel gasket. The diameter of the gasket hole is 250 μm, with 70 μm thickness chosen to avoid bridging of the single crystal at the highest applied pressure.

Finally, in Fig. 9 we show the measurements obtained at the highest applied field and pressure at low temperature. Similar to the measurements at ambient pressure we do not observe any possible magnetic contribution, as the fitted hyperfine field 7.14(6) T matches the applied one within error bar with a very small residual one.

APPENDIX B: ELECTRICAL RESISTIVITY MEASUREMENTS

Resistance of enriched sample as a function of temperature was measured in the four contact geometry down to 4.2 K with an excitation current of 100 μA using a custom build He^4 cryostat. Resistance was measured using several other excitation currents in order to check the effect of current on the superconducting transition and normal-state resistance behavior.

Figure 10(a) shows the measured resistance of LaFeSiH single crystal as a function of temperature, which shows a residual ratio resistivity $R(300\,\text{K})/R(11\,\text{K})$ of ≈25. Except the superconducting transition, no anomaly, in particular no change of slope which could suggest the onset of an antiferromagnetic state above the superconducting transition temperature is visible.

To further highlight a possible small change of slope, in Fig. 10(b), we plot the derivative of the resistance data as a function of temperature. The very sharp superconducting transition ($T_c^{90\%} - T_c^{10\%} = 0.6$ K) is shown in inset. The $T_c^{\text{Onset}} \approx 10.5$ K is slightly above the average of the whole batch used in Mössbauer experiments. However, no other signal is detected, contrary to, e.g., LaFeAsO, where a clear maximum in the derivative of the resistance is detected at the antiferromagnetic transition, as shown in Ref. [26]. No significant differences were found in the normal-state resistivity with different applied current.

APPENDIX C: MAGNETIZATION MEASUREMENTS

The magnetic properties of the three different samples were probed in a Metronique Ingenierie SQUID magnetometer using the standard extraction method: the deuterated LaFeSiD sample (analyzed by neutron powder diffraction and X-ray diffraction) and both LaFeSiH samples made of natural Fe (for NMR and Mössbauer experiments) and enriched with ^{57}Fe (for Mössbauer spectroscopy). Magnetization as a function of applied field [$M(H)$ curves] was measured at fixed temperature (2 and 150 K). Magnetization versus temperature [$M(T)$ curves] was also acquired at different applied fields (10 Oe, 100 Oe, and 1 kOe) after cooling the samples down to 2 K in zero field, measuring during heating [zero-field cooled (ZFC) process] and cooling [field cooled (FC) mode] of the sample.

The superconducting state is clearly identified in both $M(T)$ and $M(H)$ curves for the different samples, either made from natural Fe or enriched with ^{57}Fe. The $M(H)$ curve (Fig. 11 for LaFeSiD) shows the expected initial negative slope related to the diamagnetic shielding (at low field, see the linear dependence in the inset of Fig. 11). From this slope we conclude that superconductivity is bulk in the sample, with a superconducting volume fraction above 80% at 2 K for LaFeSiD. Similar or slightly higher values are found for the LaFeSiH samples. The onset of superconductivity (at 10 Oe) is found in the $M(T)$ curve at the critical temperature $T_c \approx 10$ K for LaFeSiD (see inset of Fig. 12), at $T_c \approx 8.8$ K for the enriched ^{57}Fe LaFeSiH batch (see inset of Fig. 13 for the powder and Fig. 14 for the single crystal), and at $T_c \approx 8.5$ K for LaFeSiH based on natural Fe [$M(T)$ curve not shown]. All these values are very close to the previously reported T_c values for LaFeSiH powder and single-crystal samples [7].

In the normal state, no significant anomaly is detected, except the ferromagnetic transition associated with the minor deuterated $La(Fe_{1-x}Si_x)_{13}D_y$ phase, which presents a Curie temperature near the maximal reached temperature, 320 K [46,47] (Fig. 12). From the saturated magnetization of this impurity, one can estimate that our sample contains a weight fraction less than ≈2% of such phase, which is not detected in our diffraction experiments. The presence of such ferromagnetic background could maybe hide a less-pronounced transition (like an antiferromagnetic transition) associated

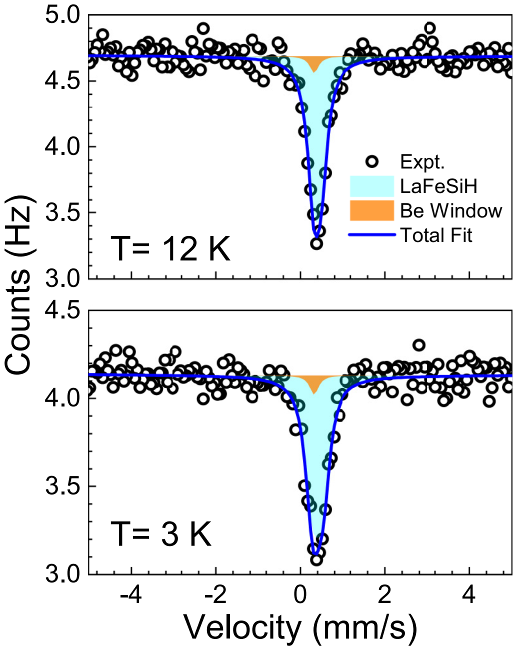

FIG. 7. Synchrotron ^{57}Fe Mössbauer raw data of LaFeSiH natural iron sample at 11.80(5) K (normal state) and 2.96(5) K (superconducting state) at ambient pressure as in Fig. 1. The spectra accumulation times were 1061 s at 3 K and 852 s at 12 K. Same symbols and color code as in Fig. 1.

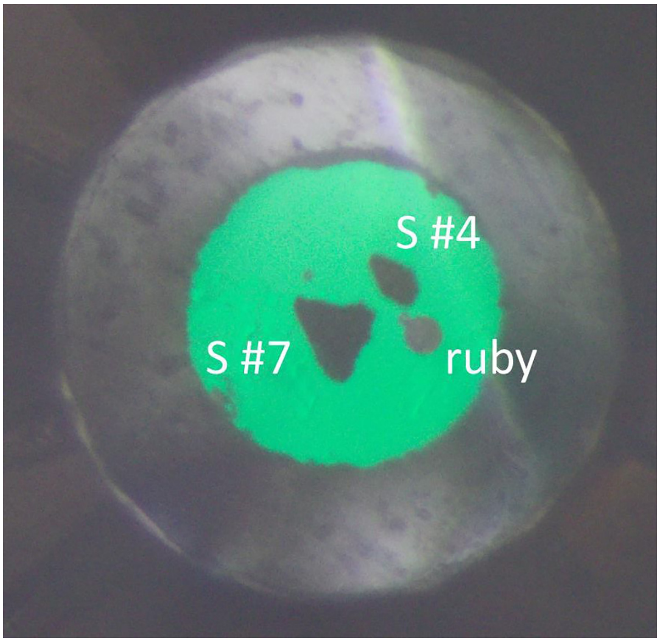

FIG. 8. Single crystals S #4 with 96% ^{57}Fe substitution and S #7 with natural iron loaded in the high-pressure cell, together with the ruby pressure gauge.

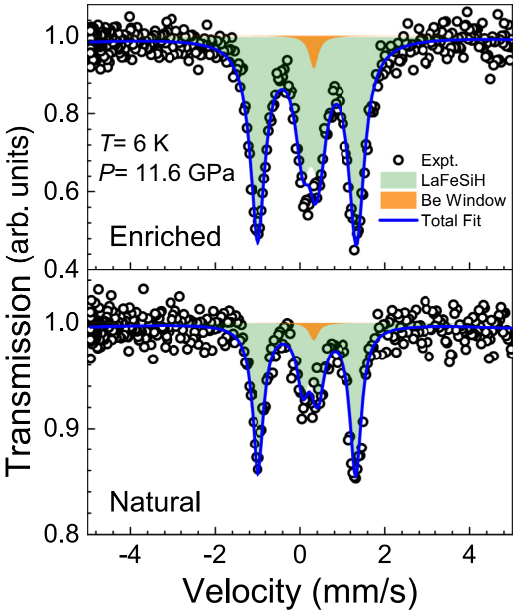

FIG. 9. SMS spectra of LaFeSiH enriched (top panel) and natural (bottom panel) sample at $H = -7\,\mathrm{T}$, $T = 6\,\mathrm{K}$ and $P = 11.4\,\mathrm{GPa}$. Same symbols and color code as in Fig. 2(a).

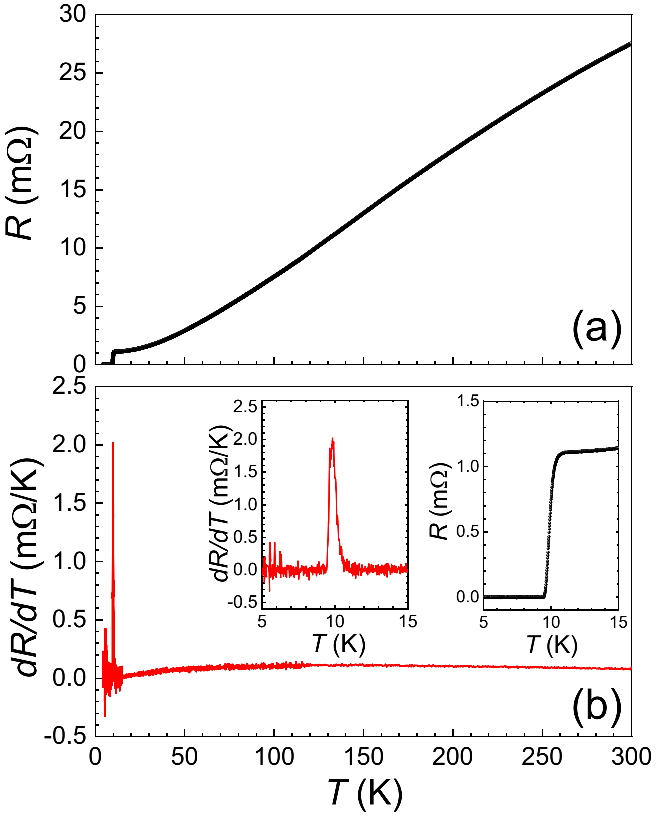

FIG. 10. (a) Resistance of LaFeSiH single crystal as a function of temperature. (b) Derivative of the resistance as a function of temperature. (Inset) Zoom for temperature range 5–15 K showing superconducting transition around 10 K.

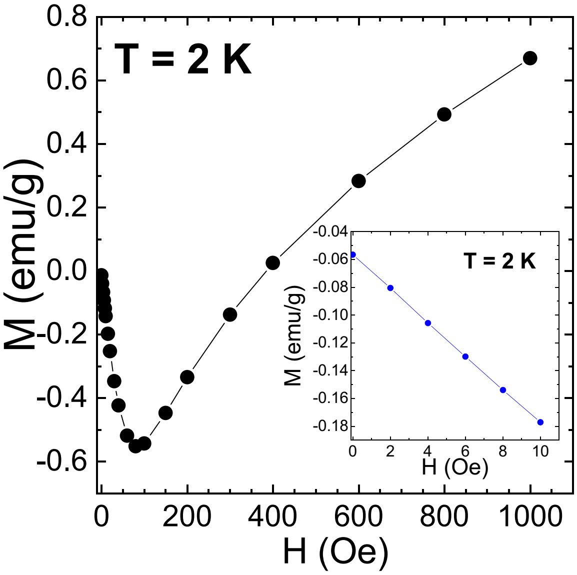

FIG. 11. Magnetic field dependence of LaFeSiD magnetization at $T = 2$ K up to 1 kOe. Inset shows magnetization at $T = 2$ K up to 10 Oe.

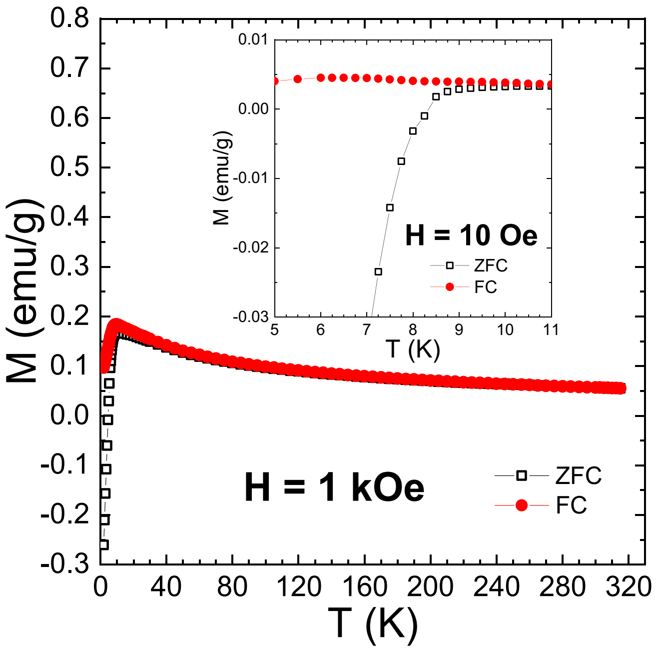

FIG. 13. Temperature dependence of isotopic ^{57}Fe-based LaFeSiH (powder) magnetization at 1 kOe up to 315 K. Inset shows enlarged view of $M(T)$ measured at 10 Oe around $T_c \approx 8.8$ K.

with the LaFeSiD main phase. In the ^{57}Fe-based LaFeSiH, this magnetic background is much smaller [see $M(T)$ curves at 1 kOe, Figs. 12 and 13) and the signature of potential $\mathrm{La(Fe_{1-x}Si_x)_{13}H_y}$ impurity is not detected or its Curie temperature is pushed largely above 315 K. Thanks to this smaller background, the Curie-Weiss behavior of the main phase becomes visible and a modelization by $\chi = \chi_0 + C/(T - \theta_W)$ gives $\theta_W \approx -69$ K, highlighting the antiferromagnetic

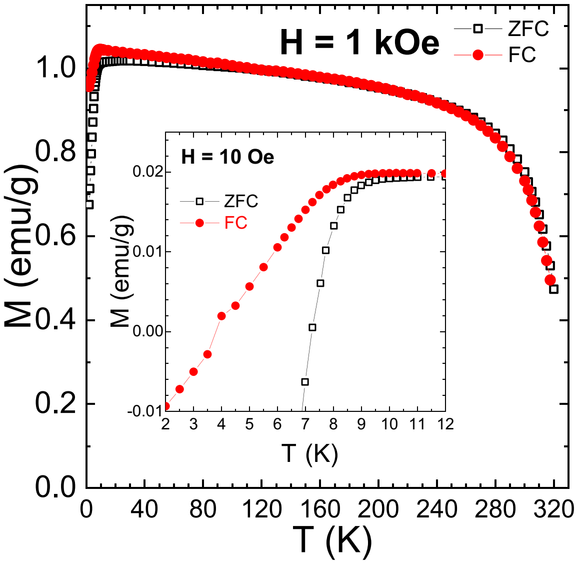

FIG. 12. Temperature dependence of LaFeSiD magnetization at 10 Oe up to 320 K. Inset shows enlarged view around $T_c = 10 \pm 0.2$ K.

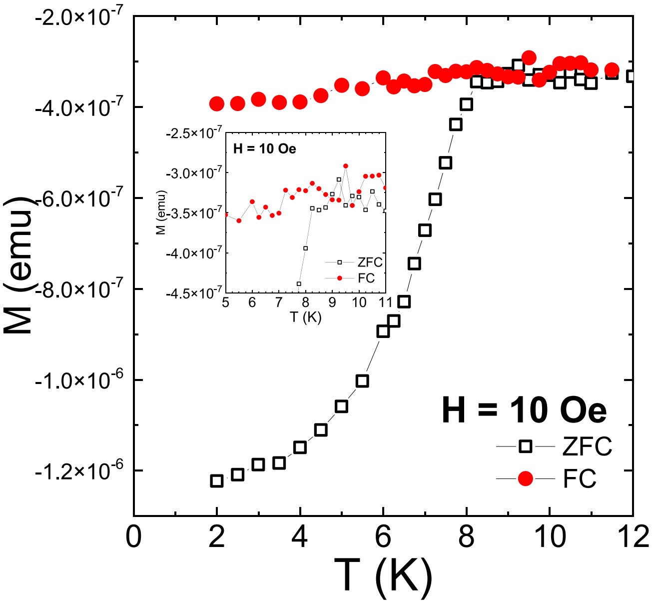

FIG. 14. Temperature dependence of isotopic ^{57}Fe-based LaFeSiH (single crystal) magnetization at 10 Oe in the 2–12 K range. Inset shows enlarged view of $M(T)$ measured at 10 Oe around T_c.

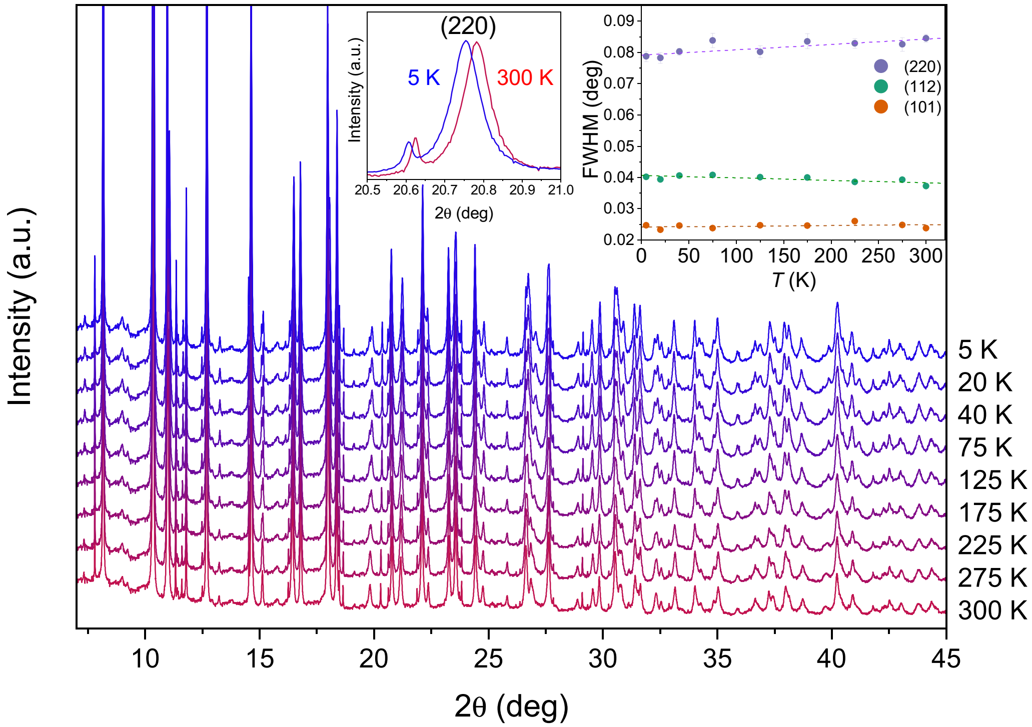

FIG. 15. XRD patterns of LaFeSiD collected at SOLEIL at different temperatures using a Mythen 2 detector, showing no splitting of peaks down to 5 K. The insets shows a zoom of the (220) peak at 300 and 5 K, clearly showing no splitting nor asymmetric broadening, and the FWHM of three peaks as a function of temperature. Here the (220) and (112) peaks are expected to split upon a symmetry lowering structural transition into an orthorhombic setting, whereas the (101) peak would not exhibit any such splitting. Comparing the temperature dependence of the three peaks it is evident that none of them show any anomalous behavior and indeed they have very similar temperature dependence, suggesting that the symmetry is robust with temperature.

character of the main magnetic interactions in LaFeSiH. We notice also that, except superconductivity, no other anomaly associated with potential structural, electronic, or long-range magnetic order is directly detectable in the 2–315 K range. Other complementary techniques sensitive to magnetism have been used in this work to probe such potential local or long-range magnetic order: NPD, Mössbauer, and NMR spectroscopies.

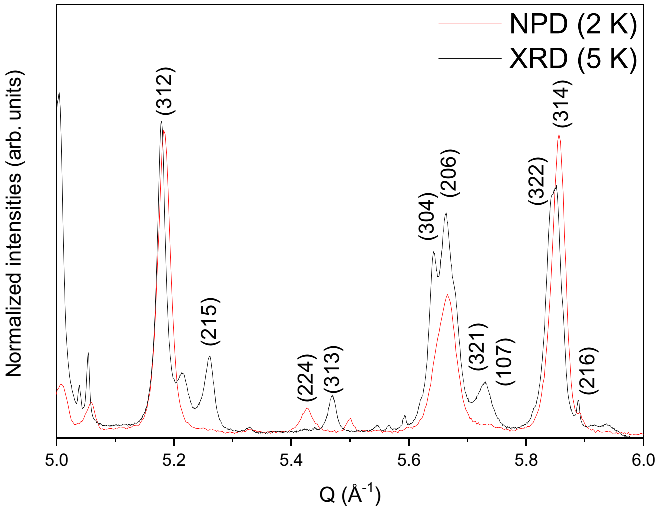

FIG. 16. Comparison of the neutron and X-ray powder diffraction data at large Q range for LaFeSiD powder collected at base temperature at ILL and SOLEIL, respectively.

APPENDIX D: X-RAY AND NEUTRON DIFFRACTION: COMPARISON

The deuterated sample LaFeSiD was measured using both neutron- and X-ray diffraction (see XRD patterns in Fig. 15). The comparison of diffraction patterns in Fig. 16 (at 2–5 K as an example) shows the higher resolution power of our XRD experiment compared with NPD.

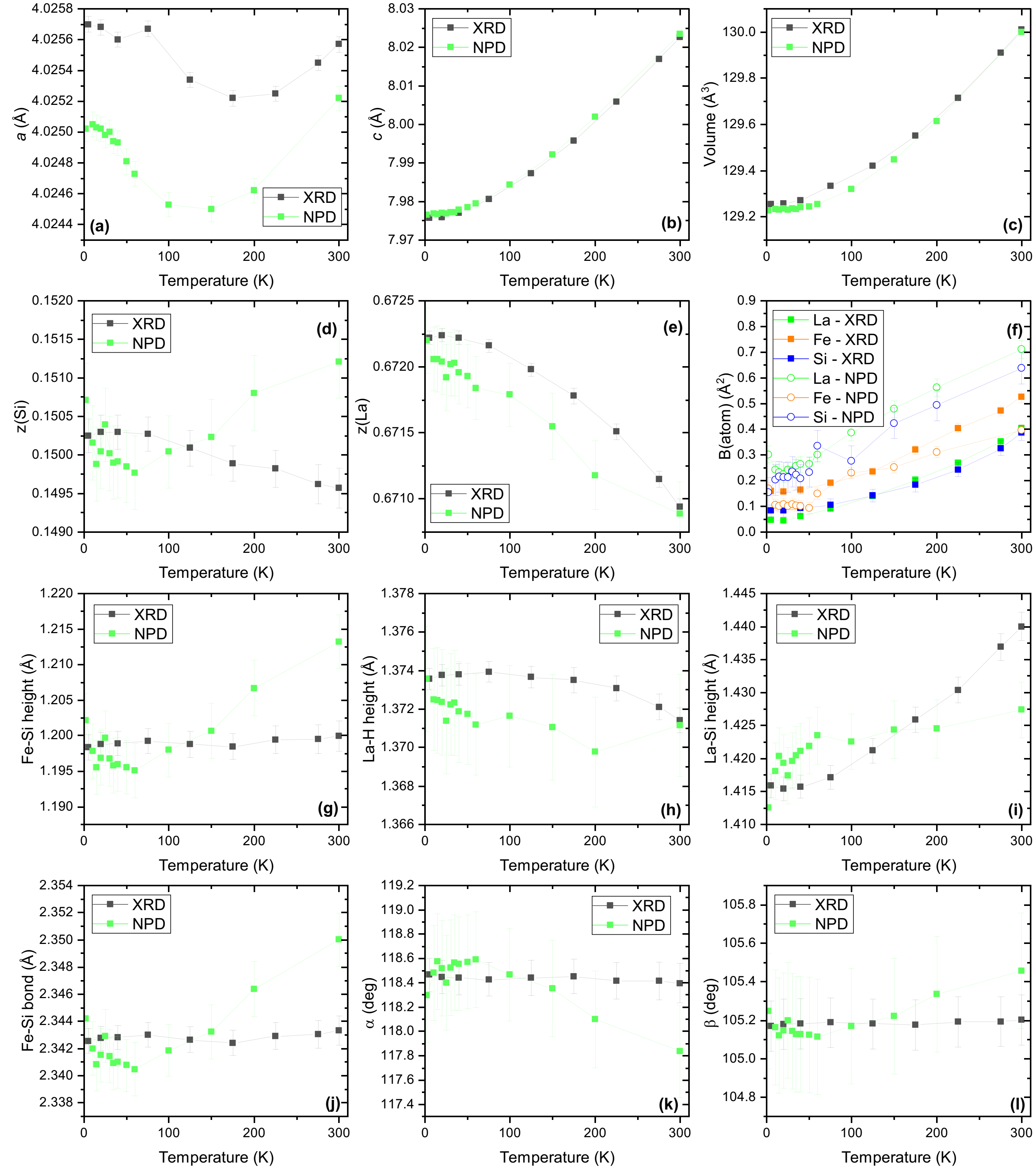

FIG. 17. Refined and calculated structural parameters for LaFeSiD as a function of temperature, measured using XRD and NPD. (a) The unit-cell parameter *a*. (b) The unit cell parameter *b*. (c) The unit-cell volume. (d) The atomic position parameter *z*(Si). (e) The atomic-position parameter *z*(La). (f) The thermal vibration parameters *B*. For deuterium, the values are in the range of 1.3 Å^2 for the NPD data and they were not refined for the XRD data. (g) The Fe-Si height, along the *c* axis. (h) The La-H(D) height along the *c* axis. (i) The La-Si height along the *c* axis. (j) The Fe-Si bond length. (k) *α* angle of the Fe-Si tetrahedron. (l) The *β* angle of the Fe-Si tetrahedron.

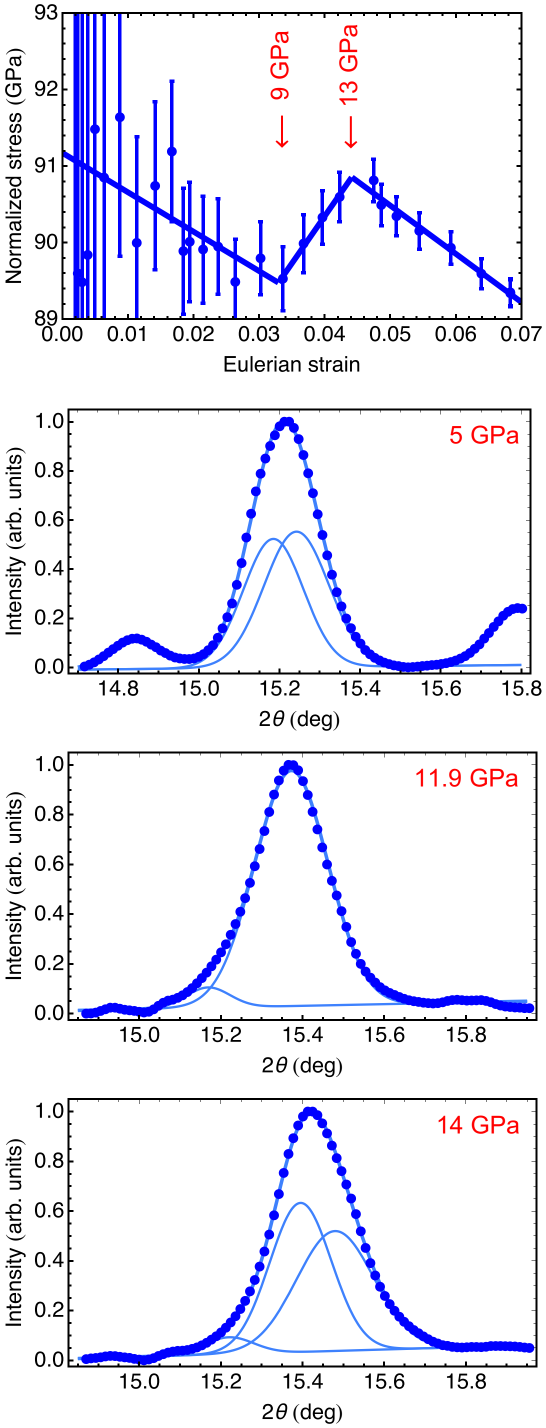

FIG. 18. (top) Equation of state for LaFeSiH at 15 K according to the XRD data measured for Ref. [7]. The Eulerian strain is defined as $f = [(V_0/V)^{2/3} - 1]/2$ while the normalized stress is $F = P/[3f(1+2f)^{5/2}]$, where (V/V_0) and P are the relative volume and the pressure respectively ($V_0 = 129.8$ Å^3). The rest of the plots show the (220) Bragg peak measured at 15 K at different pressures for Ref. [7]. This peak is slightly asymmetric at 5 and 14 GPa, but not at 11.9 GPa. The best-fit curve then requires two main Gaussians for 5 and 14 GPa, while it is obtained with only one Gaussian (plus a tail) for 11.9 GPa. These two Gaussians could be interpreted as (400) and (040) Bragg peaks if the structure becomes orthorhombic. These observations were interpreted as due to (reentrant) orthorombicity in Ref. [7].

In Fig. 15, we show the XRD patterns collected at various temperatures, showing no splitting of peaks down to 5 K. In Fig. 17 we summarize the refined structural parameters and the structural parameters calculated from XRD and NPD. Looking first at Figs. 17(a)–7(c), we show the parameters associated with the unit cell. Here we see a good agreement between the XRD and NPD data, although there is a slight offset. We ascribe this offset to the lack of precision of the neutron wavelength. Then, turning to the atomic position parameters shown in Figs. 17(d)–7(f), we see that the z(Si) parameter is not excellently matched between the two experiments. This can be explained by the rather low scattering cross-section of Si with neutrons, and we thus find it suitable to trust the parameters obtained from XRD. For the z(La) parameter we find a decent match between the two experiments. The thermal parameters B all show low positive values, decreasing as temperature decreases, indicative of a reliable fit The B values for H were not refined for the XRD data, while the neutron data yielded values around 1.3 Å^2 for D. In Figs. 17(g)–7(l) we show various geometric parameters, calculated from the refined parameters. We see that the values associated with Si, show some deviation between the XRD and NPD data, as we could expect given the above argument, however, the general trends are well matched. Table I summarizes the refined structure at 300 and 5 K.

APPENDIX E: PREVIOUS CONCLUSION OF ORTHOROMBICITY

In this Appendix, we illustrate the structural analysis performed in Ref. [7] that led to the conclusion of low-temperature orthorombicity in LaFeSiH. For this, we use XRD data associated with that publication provided by the authors, which is therefore independent of the data reported in the present paper. The normalized stress F is plotted as a function of the Eulerian strain f deduced from the XRD data at 15 K in Fig. 18 (top panel). This plot reveals three regions in which the slope of the $F(f)$ function is different as indicated by the straight lines. The boundaries between these regions correspond to 9 and 13 GPa. Furthermore, the inspection of the (220) Bragg peak reveals that the shape of this peak is slightly different in these regions, as illustrated by the rest of the plots in Fig. 18. Specifically, the peak is slightly asymmetric at 5 and 14 GPa, while it is symmetric at 11.9 GPa. This seeming asymmetry was observed together a nonmonotonic change in the width of the peak, and therefore interpreted as due to the splitting of this peak as illustrated in the figure. This situation would be possible in the case of an orthorhombic crystal structure (which was refined accordingly). These observations, however, are most likely due to small chemical inhomogeneities (i.e., partial off-stoichiometry) and/or to the presence of secondary phases such as $La(Fe_{1-x}Si_x)_{13}H_y$ or $LaFe_2Si_2$, whose diffraction peaks may overlap with those of LaFeSiH.

[1] H. Hosono and K. Kuroki, Phys. C (Amsterdam, Neth.) **514**, 399 (2015).

[2] A. Martinelli, F. Bernardini, and S. Massidda, C. R. Phys. **17**, 5 (2016).

[3] S. Iimura and H. Hosono, J. Phys. Soc. Jpn. **89**, 051006 (2020).

[4] T. Yildirim, Phys. Rev. Lett. **101**, 057010 (2008).

[5] A. Cano, M. Civelli, I. Eremin, and I. Paul, Phys. Rev. B **82**, 020408(R) (2010).

[6] I. Paul, A. Cano, and K. Sengupta, Phys. Rev. B **83**, 115109 (2011).

[7] F. Bernardini, G. Garbarino, A. Sulpice, M. Nùñez-Regueiro, E. Gaudin, B. Chevalier, M.-A. Méasson, A. Cano, and S. Tencé, Phys. Rev. B **97**, 100504(R) (2018).

[8] J.-B. Vaney, B. Vignolle, A. Demourgues, E. Gaudin, E. Durand, C. Labrugère, F. Bernardini, A. Cano, and S. Tencé, Nat. Commun. **13**, 1462 (2022).

[9] M. F. Hansen, J.-B. Vaney, C. Lepoittevin, F. Bernardini, E. Gaudin, V. Nassif, M.-A. Méasson, A. Sulpice, H. Mayaffre, M.-H. Julien, S. Tencé, A. Cano, and P. Toulemonde, npj Quantum Mater. **7**, 86 (2022).

[10] L. Hung and T. Yildirim, Phys. Rev. B **97**, 224501 (2018).

[11] A. Bhattacharyya, P. Rodière, J.-B. Vaney, P. K. Biswas, A. D. Hillier, A. Bosin, F. Bernardini, S. Tencé, D. T. Adroja, and A. Cano, Phys. Rev. B **101**, 224502 (2020).

[12] P. Villar Arribi, F. Bernardini, L. de' Medici, P. Toulemonde, S. Tencé, and A. Cano, Europhys. Lett. **128**, 47004 (2020).

[13] I. I. Mazin, M. D. Johannes, L. Boeri, K. Koepernik, and D. J. Singh, Phys. Rev. B **78**, 085104 (2008).

[14] M. Hansen, J.-B. Vaney, P. De Rango, M. Salaün, S. Tencé, V. Nassif, and P. Toulemonde, J. Alloys Compd. **945**, 169281 (2023).

[15] B. Fultz, *Characterization of Materials* (John Wiley, New York, 2011), pp. 816–834.

[16] R. Lübbers, G. Wortmann, and H. F. Grünsteudel, Hyperfine Interact. **123/124**, 529 (1999).

[17] P. Adler, S. A. Medvedev, P. G. Naumov, S. Mohitkar, R. Rüffer, M. Jansen, and C. Felser, Phys. Rev. B **99**, 134443 (2019).

[18] P. Adler, S. A. Medvedev, M. Valldor, P. G. Naumov, M. A. ElGhazali, and R. Rüffer, Phys. Rev. B **101**, 094433 (2020).

[19] P. Adler, M. Reehuis, N. Stüßer, S. A. Medvedev, M. Nicklas, D. C. Peets, J. Bertinshaw, C. K. Christensen, M. Etter, A. Hoser, L. Schröder, P. Merz, W. Schnelle, A. Schulz, Q. Mu, D. Bessas, A. Chumakov, M. Jansen, and C. Felser, Phys. Rev. B **105**, 054417 (2022).

[20] V. Potapkin, A. I. Chumakov, G. V. Smirnov, J.-P. Celse, R. Rüffer, C. McCammon, and L. Dubrovinsky, J. Synchrotron Radiat. **19**, 559 (2012).

[21] G. V. Smirnov, U. van Bürck, A. I. Chumakov, A. Q. R. Baron, and R. Rüffer, Phys. Rev. B **55**, 5811 (1997).

[22] R. Rüffer and A. I. Chumakov, Hyperfine Interact. **97-98**, 589 (1996).

[23] C. Prescher, C. McCammon, and L. Dubrovinsky, J. Appl. Crystallogr. **45**, 329 (2012).

[24] S. Kitao, Y. Kobayashi, S. Higashitaniguchi, M. Saito, Y. Kamihara, M. Hirano, T. Mitsui, H. Hosono, and M. Seto, J. Phys. Soc. Jpn. **77**, 103706 (2008).

[25] Y. Mizuguchi, T. Furubayashi, K. Deguchi, S. Tsuda, T. Yamaguchi, and Y. Takano, Phys. C (Amsterdam, Neth.) **470**, S338 (2010).

[26] H.-H. Klauss, H. Luetkens, R. Klingeler, C. Hess, F. J. Litterst, M. Kraken, M. M. Korshunov, I. Eremin, S.-L. Drechsler, R. Khasanov, A. Amato, J. Hamann-Borrero, N. Leps, A. Kondrat, G. Behr, J. Werner, and B. Büchner, Phys. Rev. Lett. **101**, 077005 (2008).

[27] M. A. McGuire, A. D. Christianson, A. S. Sefat, B. C. Sales, M. D. Lumsden, R. Jin, E. A. Payzant, D. Mandrus, Y. Luan, V. Keppens, V. Varadarajan, J. W. Brill, R. P. Hermann, M. T. Sougrati, F. Grandjean, and G. J. Long, Phys. Rev. B **78**, 094517 (2008).

[28] T. Kawakami, T. Kamatani, H. Okada, H. Takahashi, S. Nasu, Y. Kamihara, M. Hirano, and H. Hosono, J. Phys. Soc. Jpn. **78**, 123703 (2009).

[29] B. W. Lebert, T. Gorni, M. Casula, S. Klotz, F. Baudelet, J. M. Ablett, T. C. Hansen, A. Juhin, A. Polian, P. Munsch, G. Le Marchand, Z. Zhang, J.-P. Rueff, and M. d'Astuto, Proc. Natl. Acad. Sci. USA **116**, 20280 (2019).

[30] B. W. Lebert, V. Balédent, P. Toulemonde, J. M. Ablett, and J.-P. Rueff, Phys. Rev. B **97**, 180503(R) (2018).

[31] D. Bessas, I. Sergueev, K. Glazyrin, C. Strohm, I. Kupenko, D. G. Merkel, G. J. Long, F. Grandjean, A. I. Chumakov, and R. Rüffer, Phys. Rev. B **101**, 035112 (2020).

[32] C. de la Cruz, Q. Huang, J. W. Lynn, J. Li, W. Ratcliff II, J. L. Zarestky, H. A. Mook, G. F. Chen, J. L. Luo, N. L. Wang, and P. Dai, Nature (London) **453**, 899 (2008).

[33] S. Layek, M. F. Hansen, J.-B. Vaney, P. Toulemonde, S. Tencé, P. Boullay, A. Cano, and M.-A. Méasson, Europhys. Lett. (2024), doi: 10.1209/0295-5075/ad3b37.

[34] T. Tabuchi, Z. Li, T. Oka, G. F. Chen, S. Kawasaki, J. L. Luo, N. L. Wang, and G.-Q. Zheng, Phys. Rev. B **81**, 140509(R) (2010).

[35] J. Yang, R. Zhou, L.-L. Wei, H.-X. Yang, J.-Q. LI, Z.-X. Zhao, and G.-Q. Zheng, Chin. Phys. Lett. **32**, 107401 (2015).

[36] L. Ma, G. F. Ji, J. Dai, J. B. He, D. M. Wang, G. F. Chen, B. Normand, and W. Yu, Phys. Rev. B **84**, 220505(R) (2011).

[37] F. L. Ning, K. Ahilan, T. Imai, A. S. Sefat, M. A. McGuire, B. C. Sales, D. Mandrus, P. Cheng, B. Shen, and H.-H. Wen, Phys. Rev. Lett. **104**, 037001 (2010).

[38] L. Ma and W.-Q. Yu, Chin. Phys. B **22**, 087414 (2013).

[39] P. Carretta and G. Prando, Riv. Nuovo Cimento **43**, 1 (2020).

[40] T. Oka, Z. Li, S. Kawasaki, G. F. Chen, N. L. Wang, and G.-Q. Zheng, Phys. Rev. Lett. **108**, 047001 (2012).

[41] R. Zhou, D. D. Scherer, H. Mayaffre, P. Toulemonde, M. Ma, Y. Li, B. M. Andersen, and M.-H. Julien, npj Quantum Mater. **5**, 93 (2020).

[42] P. Wiecki, R. Zhou, M.-H. Julien, A. E. Böhmer, and J. Schmalian, Phys. Rev. B **104**, 125134 (2021).

[43] T. Iye, Y. Nakai, S. Kitagawa, K. Ishida, S. Kasahara, T. Shibauchi, Y. Matsuda, and T. Terashima, Phys. Rev. B **85**, 184505 (2012).

[44] D. Hu, X. Lu, W. Zhang, H. Luo, S. Li, P. Wang, G. Chen, F. Han, S. R. Banjara, A. Sapkota, A. Kreyssig, A. I. Goldman, Z. Yamani, C. Niedermayer, M. Skoulatos, R. Georgii, T. Keller, P. Wang, W. Yu, and P. Dai, Phys. Rev. Lett. **114**, 157002 (2015).

[45] https://doi.ill.fr/10.5291/ILL-DATA.5-23-729.

[46] M. Phejar, V. Paul-Boncour, and L. Bessais, J. Solid State Chem. **233**, 95 (2016).

[47] S. Fujieda, A. Fujita, K. Fukamichi, Y. Yamaguchi, and K. Ohoyama, J. Phys. Soc. Jpn. **77**, 074722 (2008).